

Monte Carlo comparison of x-ray and proton CT for range calculations of proton therapy beams

N Arbor^{1,2}, D Dauvergne¹, G Dedes³, J M Létang², K Parodi³,
C T Quiñones², E Testa¹ and S Rit²

¹ Institut de Physique Nucléaire de Lyon, CNRS/IN2P3 UMR5822, Université Lyon 1, 69622 Villeurbanne, France

² Université de Lyon, CREATIS, CNRS UMR5220, Inserm U1044, INSA-Lyon, Université Lyon 1, Centre Léon Bérard, France

³ Ludwig-Maximilians-Universität München (LMU), 80539 München, Germany

E-mail: nicolas.arbor@iphc.cnrs.fr

Received 12 December 2014, revised 9 April 2015

Accepted for publication 17 June 2015

Published 17 September 2015



CrossMark

Abstract

Proton computed tomography (CT) has been described as a solution for imaging the proton stopping power of patient tissues, therefore reducing the uncertainty of the conversion of x-ray CT images to relative stopping power (RSP) maps and its associated margins. This study aimed to investigate this assertion under the assumption of ideal detection systems. We have developed a Monte Carlo framework to assess proton CT performances for the main steps of a proton therapy treatment planning, i.e. proton or x-ray CT imaging, conversion to RSP maps based on the calibration of a tissue phantom, and proton dose simulations. Irradiations of a computational phantom with pencil beams were simulated on various anatomical sites and the proton range was assessed on the reference, the proton CT-based and the x-ray CT-based material maps. Errors on the tissue's RSP reconstructed from proton CT were found to be significantly smaller and less dependent on the tissue distribution. The imaging dose was also found to be much more uniform and conformal to the primary beam. The mean absolute deviation for range calculations based on x-ray CT varies from 0.18 to 2.01 mm depending on the localization, while it is smaller than 0.1 mm for proton CT. Under the assumption of a perfect detection system, proton range predictions based on proton CT are therefore both more accurate and more uniform than those based on x-ray CT.

Keywords: proton therapy, proton computed tomography, Monte Carlo simulation

(Some figures may appear in colour only in the online journal)

1. Introduction

Proton radiography and computed tomography (proton CT) have been studied since the early 1960s (Cormack 1963, Koehler 1968, Steward and Koehler 1973, Hanson 1979). These techniques were ruled out by x-ray tomography in the past fifty years. Recent developments of proton and carbon therapy centers have renewed the interest in high energy charged particles as a radiological tool. The evolution of tracking and calorimetry detectors applied to high energy and nuclear physics experiments has also motivated recent studies on proton imaging (Schulte *et al* 2004, Sadrozinski *et al* 2011, Scaringella *et al* 2013).

The application of proton CT in a proton therapy treatment planning was proposed in the 1990s (Schneider and Pedroni 1995, Zygmanski *et al* 2000). Besides the possibility of using a single machine for patient imaging and treatment, a more precise reconstruction of the tissue stopping power is one of the main advantages of proton CT.

A proton therapy treatment plan aims to optimize the dose delivery to patients. Due to the steep Bragg peak fall-off of charged particles, uncertainties on proton range calculations need to be carefully translated in treatment safety margins. Relatively large margins tend to limit the therapeutic outcome of proton therapy. The main uncertainties are currently related to the limited precision of some physical quantities, e.g., the mean ionization energy used in stopping power calculations, to calibration steps required to convert x-ray planning CT images into stopping power relative to water generally called relative stopping power (RSP), and to patient positioning and anatomy (Paganetti 2012).

In the current clinical practice, dose calculations in proton therapy are computed from tissue attenuation coefficients obtained from x-ray CT images. A stoichiometric calibration (Schneider *et al* 1996) is applied to convert the x-ray CTs in RSP maps. Proton range uncertainties arising from such a conversion are difficult to quantify due to a strong tissue dependence. According to various studies, resulting range uncertainty varies from 0.8% (Matsufuji *et al* 1998, Chvetsov and Paige 2010) to 3% (Schaffner and Pedroni 1998, Yang *et al* 2012) depending if the uncertainty due to the mean ionization energy (about 1.5%) is included. Resolution of CT images, including possible x-ray CT artifacts, can also affect the accuracy of reconstructed RSP maps. Including main uncertainty sources, current proton therapy safety margins on ion ranges are between 2.5%+1 mm and 3.5%+3 mm depending on the proton center (Paganetti 2012).

Proton CT has the potential to improve the accuracy of proton therapy treatments by a direct reconstruction of RSP maps. Another potential benefit is the reduction of imaging doses compared to x-ray CT. Several studies have already demonstrated the capability of proton imaging to reconstruct tissue RSP at a high resolution (Schulte *et al* 2005, Depauw and Seco 2011). However, the quantification of the improvement with respect to x-ray CT is still missing.

This study aims at quantifying the theoretical accuracy of RSP maps reconstructed from proton CT and the impact on the prediction of proton ranges. We have developed a Monte Carlo simulation framework based on Geant4 (Agostinelli *et al* 2003) to compare proton therapy dose maps computed from an x-ray or a proton CT scanner. This framework followed the main steps of a clinical treatment plan, i.e. proton or x-ray CT imaging with ideal detection systems, RSP maps reconstruction based on the scanner calibration using a tissue-equivalent phantom and calculations of the proton dose maps. A computational phantom of a human was used for imaging and for proton dose calculations. The resulting dose maps were compared to evaluate the interest of proton CT in the planning of proton therapy.

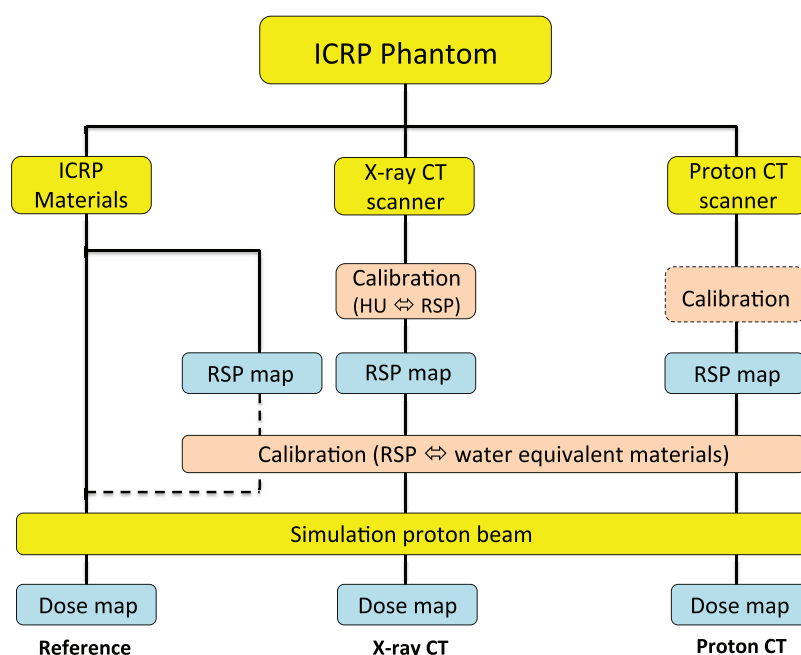


Figure 1. Schematic view of the Monte Carlo framework detailed throughout section 2. Dashed lines indicate steps that have been tested but were eventually found to be unnecessary.

2. Materials and methods

A simulation toolkit was used to simulate a proton treatment from patient imaging to dose deposit. This *in silico* study relied on GATE v6 (Jan *et al* 2011), a Monte Carlo software based on Geant4 version 9.5.p02. Dose maps computed on simulated x-ray and proton CT images were compared to a common reference. A schematic summary of the study framework is shown in figure 1 and detailed in the following sections.

2.1. Virtual patient

The anatomy of the virtual patient was that of the human-tissue computational phantom of the International Commission on Radiological Protection (ICRP) (ICRP 2009). ICRP phantoms include the positions and the chemical compositions of the organs of male and female subjects. We used the female phantom which is better resolved (voxel size of $1.775 \times 1.775 \times 4.84$ mm³). Three anatomical sites were selected to include a large distribution of tissue densities and compositions: the head, the lungs, and the liver regions. The phantom was put in a vacuum medium for the full analysis including imaging and dose simulations.

2.2. Reference map

The materials map of the ICRP phantom was converted to a RSP map of 300 MeV protons using the Geant4 stopping power table produced during the initialization of the simulation (Wright 2013). This RSP conversion is based on material compositions and densities. The

map was resampled to the same isotropic $1 \times 1 \times 1 \text{ mm}^3$ voxel size using nearest-neighbor interpolation for consistency with the simulated x-ray and pCT images. Reference dose maps were computed from the energy deposition in defined ICRP materials. Proton beam simulations used to estimate reference proton ranges are described in section 2.5.

2.3. X-ray CT

The simulated x-ray CT scanner was described in the GATE framework as a flat panel and a realistic polychromatic cone-beam, positioned at 100 cm from the isocenter. The photon energy distribution of the source in GATE was generated with SpekCalc (Poludniowski *et al* 2009) using a 120 kV voltage. The detector response, which corresponds to the detected energy as a function of the incident energy, was that of a CsI scintillator (Roberts *et al* 2008) with a $533 \times 67 \text{ mm}^2$ size at the isocenter. The source trajectory was a circle with 1° steps. To speed up the simulation process, Digitally Reconstructed x-ray Radiographs (DRRs) were produced using a GATE module for deterministic simulation based on ray-casting of the attenuation coefficient maps at each energy. Scattered particles were not considered in the simulation to approximate ideal conditions with antiscatter grids. The defined system is a realistic scanner with known characteristics for beam-hardening correction and perfect scatter correction. X-ray CT images were reconstructed using a 2D filtered backprojection algorithm with a voxel size of $1 \times 1 \times 1 \text{ mm}^3$ after a pre-correction for beam hardening using a lookup table describing water-equivalent thickness.

A deterministic x-ray simulation corresponds to a perfect image produced with an infinite dose. Realistic radiographs were obtained by adding statistical noise. The expected number of photons in each pixel was computed and Poisson noise added accordingly. The relation between the number of photons and the dose to the patient has been established using a variance reduction technique already integrated to the GATE framework (Smekens *et al* 2009, 2014) and used to adjust the x-ray imaging dose. A dose criterion based on the image dose maps and the corresponding dose-volume histograms has been chosen to deliver similar doses with both x-ray and proton CT. The dose-volume criterion was the patient volume that received 1 mGy or more.

A clinical Gammex 467 tissue characterization phantom was simulated to produce the x-ray calibration curve required to convert Hounsfield units into RSP. This phantom is made of a 33 cm diameter cylinder of solid water with sixteen 2.8 cm diameter inserts of various tissue equivalent materials (figure 2). The RSPs of the inserts were computed using Geant4 for a 300 MeV proton beam. Compositions, physical densities, stopping powers and RSPs obtained for the Gammex materials are listed in tables 1 and 2 (Landry *et al* 2013).

The RSP maps obtained from x-ray CT images rely on the calibration curve that converts Hounsfield units into RSP. Two different approaches were tested to determine the impact of the calibration on the reconstructed RSP maps. The first calibration approach corresponded to a linear interpolation of the reconstructed values of the Gammex 467 phantom. The second calibration approach corresponded to a least-squares adjustment using two linear functions. The use of this RSP map in the treatment simulation is described in section 2.5.

2.4. Proton CT

Proton CT reconstructs RSP maps from the measure of the energy loss of protons through the object. The stopping power $\frac{dE}{dx}$ is generally approximated by the Bethe-Bloch equation

$$-\frac{dE}{dx}(\vec{r}) = \rho_e(\vec{r})F(I(\vec{r}), E(\vec{r})) \quad (1)$$

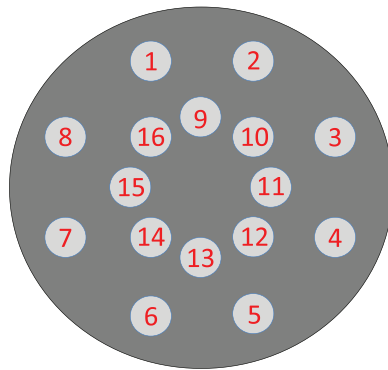


Figure 2. Gammex 467 phantom configuration. The index-to-material mapping is provided in table 2.

Table 1. Compositions of the materials of the Gammex 467 calibration phantom.

	^1H (%)	^6C (%)	^7N (%)	^8O (%)	^{12}Mg (%)	^{14}S (%)	^{15}P (%)	^{17}Cl (%)	^{20}Ca (%)
LN300 lungs	8.46	59.38	1.96	18.14	11.19	0.78	0	0.10	0
LN450 lungs	8.47	59.57	1.97	18.11	11.21	0.58	0	0.10	0
AP6 adipose	9.06	72.3	2.25	16.27	0	0	0	0.13	0
BR12 breast	8.59	70.11	2.33	17.90	0	0	0	0.13	0.95
Water solid CT	8.00	67.30	2.39	19.87	0	0	0	0.14	2.31
Water insert	11.20	0	0	88.80	0	0	0	0	0
BRN-SR2 brain	10.83	72.54	1.69	14.86	0	0	0	0.08	0
LV1 liver	8.06	67.01	2.47	20.01	0	0	0	0.14	2.31
IB inner bone	6.67	55.64	1.96	23.52	0	0	3.23	0.11	8.86
B200 bone mineral	6.65	55.52	1.98	23.64	0	0	3.24	0.11	8.87
CB2-30% CaCO₃	6.68	53.48	2.12	25.61	0	0	0	0.11	12.01
CB2-50% CaCO₃	4.77	41.63	1.52	32.00	0	0	0	0.08	20.02
SB3 cortical bone	3.41	31.41	1.84	36.50	0	0	0	0.04	26.81

where ρ_e is the electron density and F is a function of the ionization energy map I and the proton energy E (Amsler and others Particle Data Group 2014). In proton CT, equation (1) is used to relate the energy loss $\Delta E = E_{\text{in}} - E_{\text{out}}$ of protons with the integral of the RSP along a 3D path \vec{F} of length L . The reconstruction problem is formulated by the integral of proton RSP over the full proton path L , generally called the Water Equivalent Path Length (WEPL)

$$\text{WEPL} \equiv \int_{E_{\text{in}}}^{E_{\text{out}}} \frac{1}{dE/dx_w(E)} dE \simeq \int_L \frac{dE/dx}{dE/dx_w} (\vec{F}(l)) d\vec{F}(l). \quad (2)$$

This equality would be exact if the map of proton stopping power relative to the proton stopping power of water was constant with the proton energy. This assumption is verified with less than 0.7% variations for Gammex 467 materials in the 80–300 MeV energy range (figure 3, right). By making the approximation that the ionization energy is spatially constant and equal to that of water, i.e. $I(\vec{F}(l)) \simeq I_{\text{water}}$, the reconstructed image can also be considered as a map of tissue relative electron density

Table 2. Densities, stopping powers and RSPs of the materials of the Gammex 467 calibration phantom for a 300 MeV proton beam. Inserts position is described in figure 1.

Insert ID	Materials	Density (g·cm ³)	dE/dx (MeV·cm ⁻¹)	RSP
5	LN300 lungs	0.30	1.023	0.291
6	LN450 lungs	0.45	1.552	0.442
3,15	AP6 adipose	0.94	3.314	0.943
13	BR12 breast	0.98	3.412	0.971
8,11	Water solid CT	1.02	3.506	0.998
10	Water insert	1.00	3.513	1.000
9	BRN-SR2 brain	1.05	3.726	1.060
2,16	LV1 liver	1.10	3.755	1.068
1	IB inner bone	1.14	3.808	1.083
4	B200 bone mineral	1.15	3.843	1.093
7	CB2-30% CaCO₃	1.34	4.468	1.271
12	CB2-50% CaCO₃	1.56	5.051	1.437
14	SB3 cortical bone	1.82	5.733	1.631

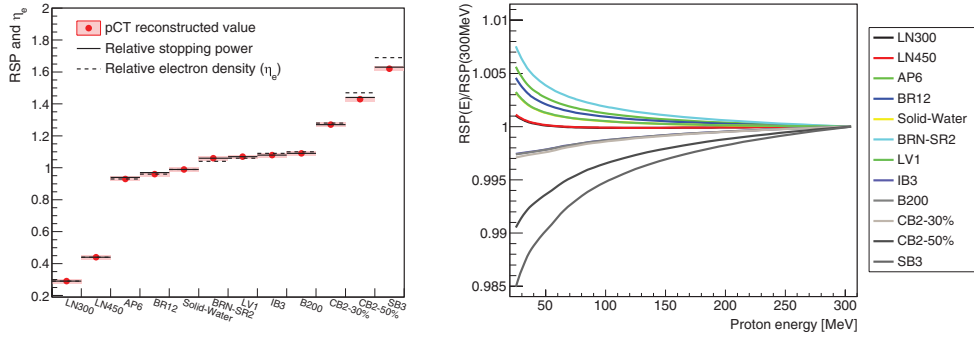


Figure 3. Left: reconstructed values of Gammex 467 materials in proton CT images compared to theoretical relative electron density and RSP. Right: Geant4 relative stopping power of Gammex 467 materials, divided by the 300 MeV value, as a function of the proton energy.

$$\int_L \frac{dE/dx}{dE/dx_w}(\vec{\Gamma}(l))dl \simeq \int_L \frac{\rho_e}{\rho_{e,w}}(\vec{\Gamma}(l)) \frac{F(I(\vec{\Gamma}(l))) = I_{water}, E(\vec{\Gamma}(l)))}{F(I_{water}, E(\vec{\Gamma}(l)))} dl = \int_L \frac{\rho_e}{\rho_{e,w}}(\vec{\Gamma}(l))dl. \quad (3)$$

The effect of the two approximations was evaluated on the Gammex 467 materials (figure 3, left) which showed that it is more accurate to consider the reconstructed image as a map of tissue RSP rather than a map of relative electron densities.

The simulated proton CT scanner corresponded to an ideal detector composed of two planes at the entrance and the exit of the phantom, to register the proton position, direction and energy before and after the patient. The proton source was a cone beam positioned at 200cm from the isocenter. The longitudinal axis of the phantom was perpendicular to the wide-angle plane of the cone beam. The two planes, of size 100 cm × 100 cm, were positioned at -80cm and 80cm with respect to the isocenter. The planes were assumed to be perfect

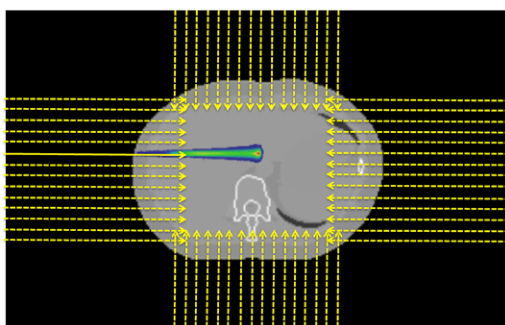


Figure 4. Illustration of proton beams configuration for dose calculations in the liver region. The dose corresponding to one of the proton beams is shown superimposed on the CT slice.

detectors, which measured the exact energy, position and momentum direction of each proton. For each simulated scan, the phantom was rotated in 360 steps of 1° and about 9×10^8 protons were used for the whole scan. The selected initial energy was 300 MeV, which corresponds to the energy required for the largest part of the ICRP phantom in order to get at least 80 MeV residual energy for the exit protons. This energy was selected to fulfill the assumption of a constant RSP with the proton energy with less than 1% variation (figure 3, right).

Due to Coulomb scattering, protons are deflected many times along their path. It has been shown that an estimate of the position and the direction of each proton (i.e. in a list mode manner) before and after the patient enables the computation of a maximum likelihood estimate of the proton trajectory known as the most likely path (MLP) (Williams 2004, Schulte *et al* 2008). In the proposed analysis, proton CT reconstruction was based on a filtered backprojection algorithm recently developed to include the MLP formalism using a distance driven binning approach (Rit *et al* 2013). Proton CT images were reconstructed using a voxel size of $1 \times 1 \times 1 \text{ mm}^3$.

The Gammex 467 calibration phantom was used to validate the accuracy of RSPs provided by proton CT. The maps were then used in the same manner as with x-ray maps to estimate their accuracy for proton dose simulations as described in the next section.

2.5. Proton range prediction

Proton pencil beams were simulated for a variety of positions and directions, without clinical considerations, to estimate the accuracy of the prediction of their range based on x-ray and proton CT. For each anatomical region (liver, head and lungs), four incident directions have been selected, spaced by a 90° angle in the axial plane (figure 4). Multiple pencil beams of initial gaussian shape ($\sigma = 5 \text{ mm}$) were simulated to reach a total width that covered the lateral size of the phantom. The beams tangent to the patient skin were discarded. The beams were perfectly mono energetic with an energy of 140 MeV for the liver and the head regions, and 100 MeV for the lungs. These energies correspond to a mean proton path of about 120 mm.

Dose maps were computed using the energy deposit in each voxel. The longitudinal projection on the beam axis of the dose distribution of each pencil beam was interpolated by a cubic spline function to avoid binning effects related to the voxel size of the ICRP phantom. Proton range was defined as the position for which the dose has decreased to 80% of the maximum dose (Paganetti 2012).

In Monte Carlo simulations, there is an uncertainty on the proton range induced by the straggling of the exit beam energy. In order to limit the impact of this uncertainty on the range

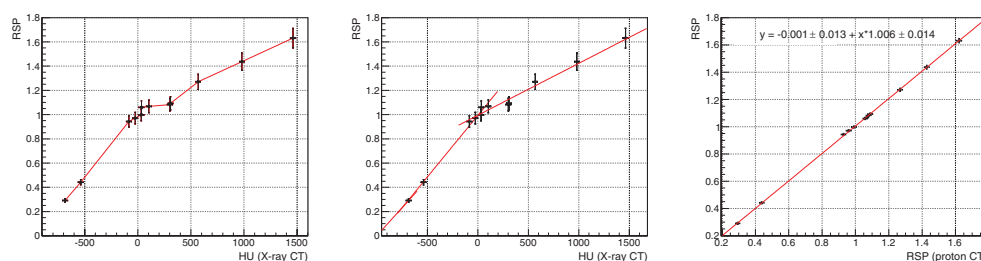


Figure 5. Calibration curves for x-ray and proton CT scanner simulations of a Gammex 467 phantom. For the x-ray CT, reconstructed values are linearly interpolated (left) or fitted with two linear functions (middle). For the proton CT, reconstructed values are fitted with a unique linear function (right).

estimate, a large number of particles have been simulated for each of the 5 mm pencil beams. The number of protons per beam has been computed to reach a statistical range uncertainty lower than 0.05 mm (1σ), which is less than 0.05% of the mean proton range, for the irradiation of a water box. This proton number was 1.5×10^6 protons per beam.

2.6. RSP to material conversion

For a proton therapy treatment plan based on Monte Carlo, reconstructed RSP maps need to be transformed into Monte Carlo materials with specific compositions and densities before applying dose calculations. This material calibration is required to produce dose maps by simulating proton interactions in the patient. In the proposed analysis, RSP maps reconstructed from x-ray and proton CT images have been transformed voxel-by-voxel into water equivalent materials. For each voxel, the water density has been adjusted in order to reach the reconstructed RSP value of the voxel.

This step could introduce some uncertainties related to wrong materials composition. This additional uncertainty should be separated from the uncertainty related to the accuracy of the RSP reconstruction process. A specific treatment plan has been developed to quantify the impact of the material composition on proton range calculations (figure 1, dashed branch). RSP maps have been produced using the ICRP phantom voxels information in the anatomical liver region. These RSP maps have then been converted into water equivalent materials by adjusting the density of each voxel. Following the same procedure as the one used for the x-ray CT and the proton CT plans, a set of pencil beams were simulated in four incident directions to compute proton ranges. The results were compared to the predictions of the reference plan based on the true ICRP materials composition. The comparison showed that range uncertainties introduced by wrong material compositions are not significant compared to the above-described range uncertainty of 0.05 mm. This result validated the use of water equivalent materials for proton range calculations in this analysis framework.

3. Results

3.1. Calibration

Calibration curves obtained with x-ray and proton CT scanner simulations of a Gammex 467 phantom can be observed in figure 5. The curves have been produced from the mean value and the standard deviation of each insert computed in a circular region (2 cm diameter) slightly

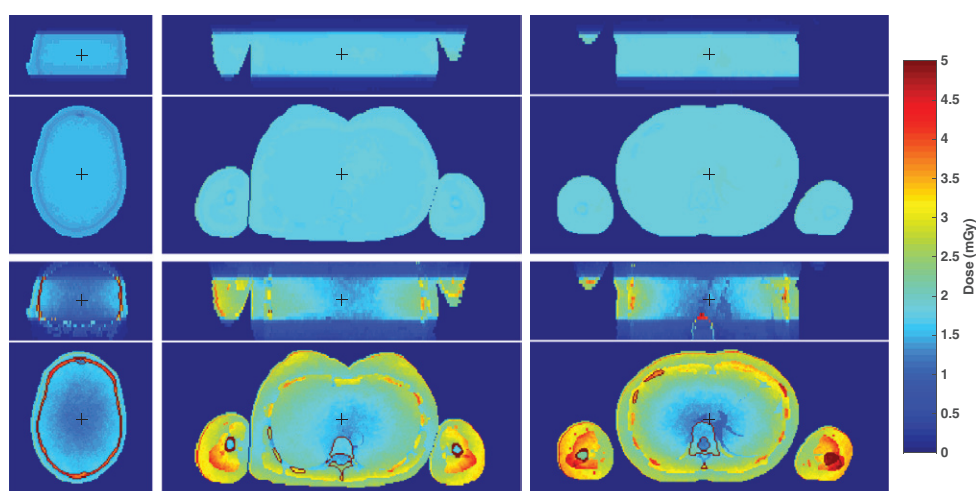


Figure 6. Spatial distribution of the dose delivered in proton (top) and x-ray (bottom) CT in mGy. For each anatomical region (head, lungs and liver), coronal and axial slices at the isocenter (black cross) are provided.

smaller than the insert size to avoid border effects. For soft tissue inserts with a Hounsfield Unit (HU) value around 0, some inserts with similar HU value have a quite different RSP.

Reconstructed values from x-ray CT have been both linearly interpolated (figure 5, left) and fitted with two linear functions in a least-squares minimization (figure 5, middle). Reconstructed values from the proton CT (figure 5, right) have been adjusted with a unique linear function close to identity which was therefore not used in the following.

3.2. Imaging dose

The dose maps of each site and each modality are provided in figure 6 and the corresponding Dose Volume Histograms (DVHs) in figure 7. The DVHs have been computed in the full patient volume of about 220 litres. Large differences can be observed between the two maps with significantly more heterogeneity in the photon dose maps and quite impressive uniformity in the proton dose maps. This translates into sharper DVHs for proton CT than x-ray CT, corresponding to a dose delivery more conformal to the imaged region. The dose criterion, i.e. the same volume receiving 1 mGy or more in both modalities, is best visualized in figure 7.

3.3. Relative stopping power maps

One slice of each RSP map is presented in figure 8. A slight blurring of proton CT images due to multiple Coulomb scattering can still be observed, despite the use of a reconstruction algorithm accounting for the most likely path of protons (Rit *et al* 2013).

Voxel-by-voxel absolute deviation of the RSP has been computed for all RSP maps. The absolute deviation of the RSP is defined as the difference between reconstructed x-ray or proton CT RSP maps and the ICRP reference map. Results for the three sites have been combined in figure 9.

Spatial uniformity of RSP deviation can also be observed in two dimensional image slices. The absolute deviation between the x-ray and proton CT RSP maps and the ICRP reference were used to produce figure 10.

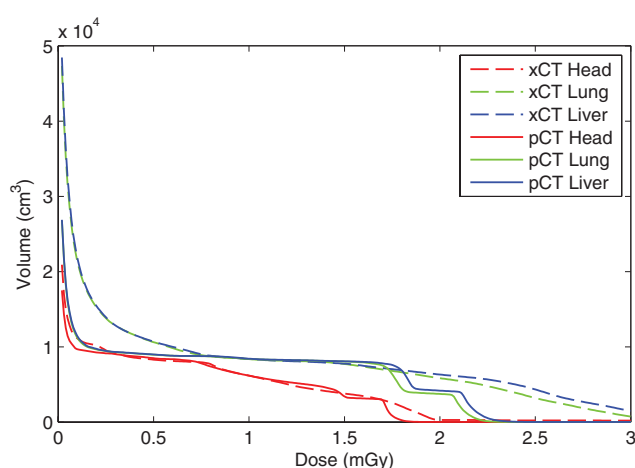


Figure 7. Dose-volume histograms of the dose delivered in proton and x-ray CT for the three anatomical sites.

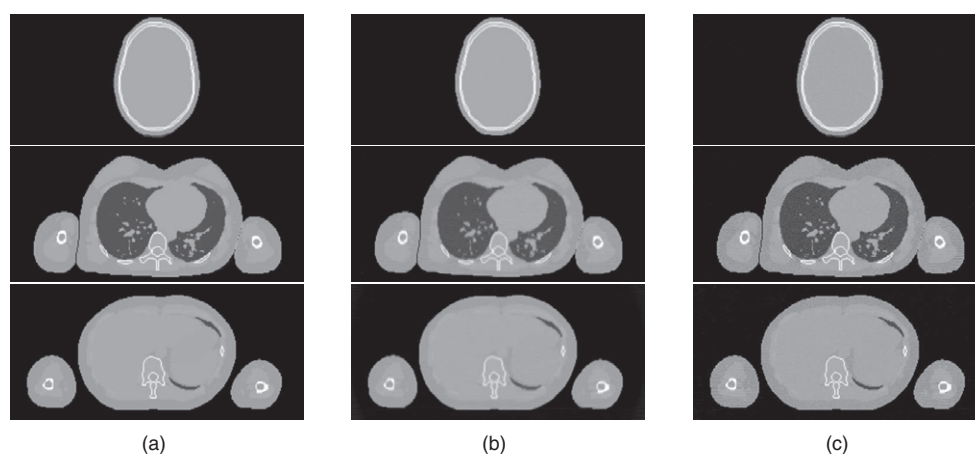


Figure 8. Example of reconstructed RSP maps for the head (top), lungs (middle) and liver (bottom) regions. Gray-level range: (0–1.708). (a) ICRP reference; (b) Proton CT; (c) x-ray CT (fit).

3.4. Proton range

Proton ranges were estimated for the three anatomical sites. X-ray and proton CT based calculations have been compared to reference proton ranges. The absolute range deviation was computed beam-per-beam and their distribution has been summarized in figure 11.

Using pencil beams with 120 mm range on average, the mean absolute deviation of the range prediction based on x-ray CT varies from 0.18 to 2.01 mm while it is smaller than 0.1 mm for proton CT. Range standard deviations are about 30% lower, and dispersions between sites are reduced from about 1 mm to less than 0.1 mm. The comparison of the two x-ray CT calibration methods highlights smaller mean range deviations with the linear interpolation but a larger dispersion between anatomical regions.

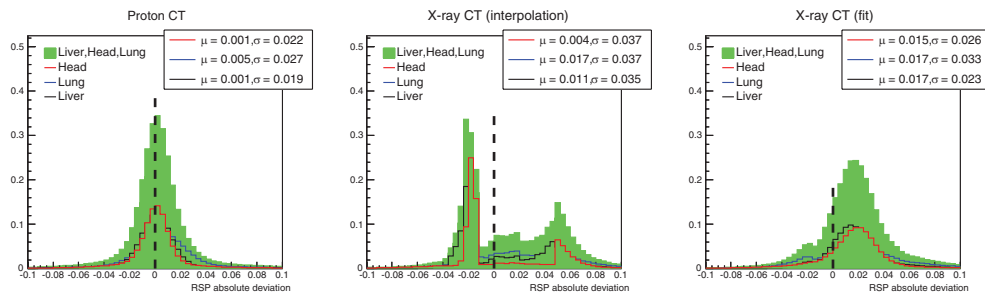


Figure 9. Distributions of the voxel-by-voxel absolute deviation of the RSP reconstructed from x-ray and proton CT with respect to the ICRP phantom reference. Absolute deviation for liver, head and lungs sites are shown for proton CT (left) and for x-ray CT with a calibration based on a linear interpolation (middle) and a fit with two linear functions (right).

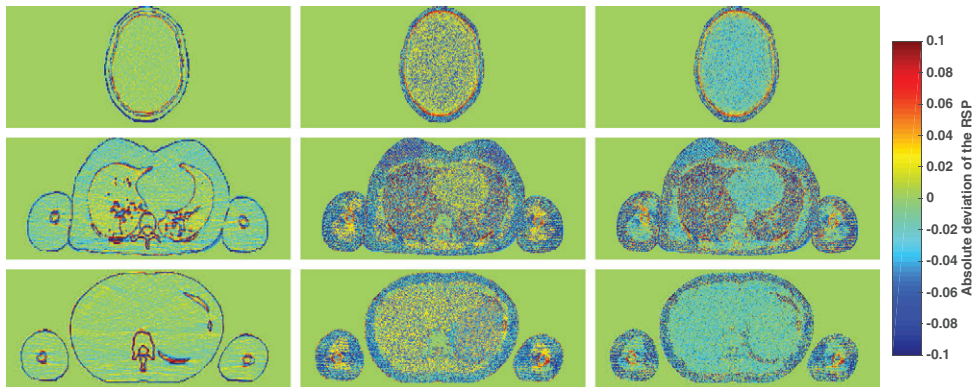


Figure 10. Two-dimensional RSP absolute deviation with respect to the ICRP reference of the proton CT (left) and x-ray CT with a calibration based on a linear interpolation (middle) and a fit with two linear functions (right) applied to the head (top), lungs (middle) and liver (bottom) sites.

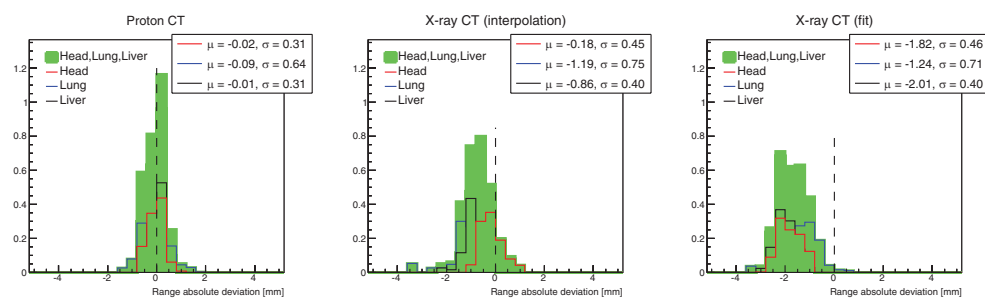


Figure 11. Absolute deviation of the proton range calculations. Absolute deviation for liver, head and lungs cases are shown for the proton CT (left) and for the x-ray CT with a calibration based on a linear interpolation (middle) and a fit with two linear functions (right).

4. Discussion

We have developed a Monte Carlo framework to estimate the accuracy and the precision of the simulation of proton dose deposits. The main steps of a conventional dose simulation, i.e. scanner calibration, RSP maps reconstruction and dose calculations, have been reproduced and analyzed to assess the performances of proton CT imaging for an ideal detection system. Proton CT has been compared to the corresponding results obtained with an x-ray CT scanner without scattering. A higher accuracy of the proton CT has been observed, both for the RSP reconstruction and for the range predictions.

Two different calibrations of x-ray CTs to RSP maps have been tested (figure 5, left and middle). Linear interpolation was selected as one of the most basic methods in order to avoid the effect of outliers. The fact that two materials with different RSPs can correspond to a similar HU value will necessarily introduce some deviations in the reconstructed RSP. Least-squares minimization was selected to improve the calibration by limiting a too strong tissue dependence. The mean deviation for a given anatomical slice will depend on the quality of the adjustment for the most frequent tissues. The impact on proton range prediction is difficult to anticipate. The mean range deviation could be small if the RSP deviations balance each other along the proton beam, or quite large if they deviate in the same direction. The use of a more complex method based on a stoichiometric calibration could help to further reduce the conversion error (Schneider *et al* 1996). However, the stoichiometric calibration is based on ICRP materials that are also used in the ICRP phantom and its use would have unrealistically favoured x-ray CT. More advanced parameters, e.g. the number of inserts used for the calibration (Jiang *et al* 2007, Bazalova and Graves 2011), have not been tested in this analysis but inter-patient variability and related uncertainty on tissue composition limits the potential of such calibrations (Yang *et al* 2012).

As expected from the Gammex 467 phantom analysis (figure 3, left), proton CT enables a precise direct derivation of tissue RSP (figure 5, right). Assuming that the scanner is perfectly calibrated, no calibration will be required for a proton therapy treatment plan based on proton CT. Besides making the process easier, avoiding calibration could help to limit uncertainties related to x-ray CT images artifacts like beam hardening or metal implant streaks.

The energy of the proton beam used in this study was 300 MeV to cross the thickest parts of the ICRP phantom with clinically acceptable doses while still providing a high enough residual energy to validate the hypothesis of constant RSP with respect to water. Although quite rare at this time, this energy should be accessible by future proton therapy systems (e.g. ProTOM Radianc 330). A lower beam energy, around 200 MeV, would be sufficient for thinner anatomical sites such as the head region. One of the advantages of using a lower proton energy in thinner regions is to decrease proton imaging dose for a similar RSP resolution (Schulte *et al* 2005). If the highest possible energy of the proton beam is not sufficient to image the patient, it is still possible to acquire proton CT images if it is combined with x-ray cone-beam CT (Hansen *et al* 2014).

Despite a similar dose level used to produce x-ray and proton CT images, spatial distributions of the delivered dose appeared quite different (figures 6 and 7). Proton dose maps displayed an impressive uniformity compared to photon dose maps. This uniformity is due to the linearity of the proton dose before the Bragg peak. Due to this linearity, the combination of opposite beams results in a spatially uniform dose distribution. The dose in the coronal slices has a sharp fall-off in proton CT whereas the dose due to secondary radiations is not negligible outside the photon beam. The possibility to constrain the dose delivered by a scanner to the primary beam region could be of great interest for patient radiation protection in regions close to organs at risk, e.g. breast tissue of a young female patient with lymphomas or head and neck cancers close to the eyes region.

A comparison of the RSP maps obtained with x-ray and proton CT showed that proton CT enables a more accurate RSP reconstruction of all anatomical sites (figure 9, left). Mean RSP absolute deviations are between 3 and 17 times larger for the x-ray CT, depending on the calibration method and the anatomical region. Spatial distribution of the RSP deviation shows that the accuracy of proton CT reconstruction is relatively uniform. This weaker tissue dependence could help to produce a more robust estimate of the proton range between patients. Larger deviations correspond to borders separating two tissues with a quite different RSP. The spatial resolution of proton CT images could explain this. As expected from previous results, x-ray CT reconstructed RSP maps are more dependent to tissue spatial distribution and reflect more the anatomical structures, particularly for the linearly interpolated calibration.

Range calculations using dose projection on the central beam axis, were not found to be significantly dependent on the material composition (section 2.6). Therefore, water equivalent materials were used in the simulated treatment planning. However, the strong atomic-number dependence of proton scattering could affect the spread of the proton beam and the related three dimensional spatial dose distribution (Paganetti 2012), especially for heterogeneous interfaces. The developed Monte Carlo framework could be used to assess the impact of material composition on proton scattering by a comparison of three dimensional proton dose maps. If the deviations were found to be significant, proton CT could also be used to measure other tissue properties than the RSP (Bopp *et al* 2013).

Proton CT enables a more accurate estimate of the proton range for all anatomical regions (figure 11). A better calculation is noticed for the mean and standard deviation of the range distributions, and for the dispersion from site-to-site. These results, obtained for ideal detectors, could form the basis of a complementary analysis including realistic detector performances. Based on the characteristics of actual proton scanners (Sadrozinski *et al* 2013, Scaringella *et al* 2013), such a simulation framework of a proton therapy treatment could be used to estimate the expected performances of proton range calculations. The parallel analysis of simulation and experimental data could also help to determine the more significant technical constraints of future scanners by directly testing the impact of energy resolution or tracking precision (Bopp *et al* 2014) on the proton range estimate.

5. Conclusion

A Monte Carlo framework has been developed to assess the theoretical performances of proton CT for the simulation of the patient dose in proton therapy. The reconstructed RSP maps with proton CT were more accurate than the RSP maps obtained from x-ray CT images. Proton range calculations based on proton CT are therefore both more precise and more uniform with a weaker dependence to the spatial distribution of tissues. Smaller treatment margins could therefore be used if proton CT was available to plan proton therapy. Proton CT also benefits from the uniformity of the imaging dose distribution and its high conformation to the primary beam region.

Acknowledgments

This work was performed within the LABEX PRIMES (ANR-11-LABX-0063) of Université de Lyon, within the program 'Investissements d'Avenir' (ANR-11-IDEX-0007) operated by the French National Research Agency (ANR), and partially supported by Lyric INCa-DGOS-4664,

France Hadron (ANR-11-INBS-0007), DEXTER (ANR-13-IS03-0002-01) and t-Gate (ANR-14-CE23-0008).

References

- Agostinelli S *et al* 2003 GEANT4: a simulation toolkit *Nucl. Instrum. Methods A* **506** 250–303
- Amsler C *et al* (Particle Data Group) 2008 The review of particle physics *Phys. Lett. B* **667** 1–6
- Bazalova M and Graves E E 2011 The importance of tissue segmentation for dose calculations for kilovoltage radiation therapy *Med. Phys.* **38** 3039–49
- Bopp C, Colin J, Cussol D, Finck C, Labalme M, Rousseau M and Brasse D 2013 Proton computed tomography from multiple physics processes *Phys. Med. Biol.* **58** 7261
- Bopp C, Rescigno R, Rousseau M and Brasse D 2014 The impact of tracking system properties on the most likely path estimation in proton CT *Phys. Med. Biol.* **59** N197–N210
- Chvetsov A V and Paige S L 2010 The influence of CT image noise on proton range calculation in radiotherapy planning *Phys. Med. Biol.* **55** N141
- Cormack A M 1963 Representation of a function by its line integrals, with some radiological applications *J. Appl. Phys.* **34** 2722–7
- Depauw N and Seco J 2011 Sensitivity study of proton radiography and comparison with kV and MV x-ray imaging using GEANT4 Monte Carlo simulations *Phys. Med. Biol.* **56** 2407
- Hansen D C, Petersen J B, Bassler N and Sørensen T S 2014 Improved proton computed tomography by dual modality image reconstruction *Med. Phys.* **41** 031904
- Hanson K M 1979 Proton computed tomography *IEEE Trans. Nucl. Sci.* **26** 1635–40
- International Commission on Radiological Protection (ICRP) 2009 ICRP Publication 110: adult reference computational phantoms *Ann. ICRP* vol 39 (Amsterdam: Elsevier) pp 3–5
- Jan S *et al* 2011 GATE V6: a major enhancement of the GATE simulation platform enabling modelling of CT and radiotherapy *Phys. Med. Biol.* **56** 881
- Jiang H, Seco J and Paganetti H 2007 Effects of Hounsfield number conversion on CT based proton Monte Carlo dose calculations *Med. Phys.* **34** 1439–49
- Koehler A M 1968 Proton radiography *Science* **160** 303–4
- Landry G, Seco J, Gaudreault M and Verhaegen F 2013 Deriving effective atomic numbers from DECT based on a parameterization of the ratio of high and low linear attenuation coefficients *Phys. Med. Biol.* **58** 6851
- Matsufuji N *et al* 1998 Relationship between CT number and electron density, scatter angle and nuclear reaction for hadron-therapy treatment planning *Phys. Med. Biol.* **43** 3261
- Paganetti H 2012 Range uncertainties in proton therapy and the role of Monte Carlo simulations *Phys. Med. Biol.* **57** R99
- Poludniowski G, Landry G, DeBlois F, Evans P M and Verhaegen F 2009 Spekcalc: a program to calculate photon spectra from tungsten anode x-ray tubes *Phys. Med. Biol.* **54** N433
- Rit S, Dedes G, Freud N, Sarrut D and Létang J M 2013 Filtered backprojection proton CT reconstruction along most likely paths *Med. Phys.* **40** 031103
- Roberts D A, Hansen V N, Niven A C, Thompson M G, Seco J and Evans P M 2008 A low z linac and flat panel imager: comparison with the conventional imaging approach *Phys. Med. Biol.* **53** 6305
- Sadrozinski H F W, Bashkirov V, Colby B and Coutrakon G 2011 Detector development for proton computed tomography (pCT) *IEEE Nuclear Science Symp. and Medical Imaging Conf. (Valencia, Spain, 23–29 October 2011)* pp 4457–61
- Sadrozinski H W, Johnson R, Macafee S, Plumb A, Steinberg D, Zatserklyaniy A, Bashkirov V, Hurley R and Schulte R 2013 Development of a head scanner for proton CT *Nucl. Instrum. Methods Phys. Res.* **699** 205–10
- Scaringella M *et al* 2013 The PRIMA (proton imaging) collaboration: development of a proton computed tomography apparatus *Nucl. Instrum. Methods Phys. Res.* **730** 178–83
- Schaffner B and Pedroni E 1998 The precision of proton range calculations in proton radiotherapy treatment planning: experimental verification of the relation between CT-HU and proton stopping power *Phys. Med. Biol.* **43** 1579
- Schneider U, Pedroni E and Lomax A 1996 The calibration of CT hounsfield units for radiotherapy treatment planning *Phys. Med. Biol.* **41** 111
- Schneider U and Pedroni E 1995 Proton radiography as a tool for quality control in proton therapy *Med. Phys.* **22** 353–63

- Schulte R *et al* 2004 Conceptual design of a proton computed tomography system for applications in proton radiation therapy *IEEE Trans. Nucl. Sci.* **51** 866–72
- Schulte R W, Bashkurov V, Loss Klock M C, Li T, Wroe A J, Evseev I, Williams D C and Satogata T 2005 Density resolution of proton computed tomography *Med. Phys.* **32** 1035–46
- Schulte R W, Penfold S N, Tafas J T and Schubert K E 2008 A maximum likelihood proton path formalism for application in proton computed tomography *Med. Phys.* **35** 4849–56
- Smekens F, Freud N, Létang J M, Adam J F, Ferrero C, Elleaume H, Bravin A, Estève F and Babot D 2009 Simulation of dose deposition in stereotactic synchrotron radiation therapy: a fast approach combining monte carlo and deterministic algorithms *Phys. Med. Biol.* **54** 4671
- Smekens F, Létang J M, Noblet C, Chiavassa S, Delpon G, Freud N, Rit S and Sarrut D 2014 Split exponential track length estimator for monte-carlo simulations of small-animal radiation therapy *Phys. Med. Biol.* **59** 7703
- Steward V W and Koehler A M 1973 Proton radiographic detection of strokes *Nature* **245** 38–40
- Williams D C 2004 The most likely path of an energetic charged particle through a uniform medium *Phys. Med. Biol.* **49** 2899
- Wright D H 2013 Geant4 physics reference manual (<http://cern.ch/geant4>)
- Yang M, Zhu X R, Park P C, Titt U, Mohan R, Virshup G, Clayton J E and Dong L 2012 Comprehensive analysis of proton range uncertainties related to patient stopping-power-ratio estimation using the stoichiometric calibration *Phys. Med. Biol.* **57** 4095
- Zygmanski P, Gall K P, Rabin M S Z and Rosenthal S J 2000 The measurement of proton stopping power using proton-cone-beam computed tomography *Phys. Med. Biol.* **45** 511